ELSEVIER

Journal of Structural Geology 27 (2005) 379–396

JOURNAL OF STRUCTURAL GEOLOGY

www.elsevier.com/locate/jsg

Effects of confinement on matrix flow around a rigid inclusion in viscous simple shear: insights from analogue and numerical modelling

F.O. Marques[a,*], R. Taborda[b], S. Bose[c], J. Antunes[d]

[a]Dep. Geologia and CGUL, Fac. Ciências, Univ. Lisboa, Edificio C6, Piso 2, 1749-016 Lisbon, Portugal
[b]Dep. Geologia and LATTEX, Fac. Ciências, Univ. Lisboa, Edificio C6, Piso 6, 1749-016 Lisbon, Portugal
[c]GEOMODELS and CGUL, Fac. Ciências, Univ. Lisboa, Edifício C8, Piso 6, 1749-016 Lisbon, Portugal
[d]Instituto Tecnológico e Nuclear, Applied Dynamics Laboratory, Estrada Nacional 10, 2686 Sacavém, Portugal

Received 19 June 2004; accepted 18 October 2004

Abstract

We use analogue and numerical modelling to show that the flow of a Newtonian viscous fluid around a rigid body, in simple shear, depends strongly on the degree of confinement, i.e. the ratio between the shear zone width (H) and the rigid inclusion's least axis (e_2) ($S=H/e_2$). It also depends on how closely we look at the inclusion, which leads to the definition of an effective channel length and an effective flow pattern, compatible with micro-tectonics observations. If we consider a long channel, the flow pattern is bow tie-shaped, but tends to become eye-shaped as S approaches infinity. If we zoom in to an effective channel no longer than 10 inclusion diameters, the flow pattern is effectively bow tie-shaped for low to medium S values, but becomes effectively eye-shaped at medium to high S values. These changes may have great influence on the geometry of tails around a rigid inclusion. Therefore, special care must be taken when trying to infer rock rheology (e.g. viscous Newtonian or non-Newtonian) from geometrical patterns (e.g. geometry of a mantle and tails of recrystallized material around a rigid body), which are assumed to reflect the flow type.

Keywords: Effective bow tie- and eye-shaped flow; Newtonian matrix; Confined simple shear; Effective channel length; Analogue and numerical experiments

1. Introduction

The rheology of the Earth's interior is typically assessed at two quite different scales: the large scale, through distributions of topography, gravity and heat flow (e.g. Davies, 1999), and the sub-microscopic scale, through evaluation of deformation mechanisms (e.g. Nicolas and Poirier, 1976). However, the first can only give us an idea of the overall behaviour of large volumes of the Earth's interior, and the second is commonly hampered by late-stage recrystallization of the rock. Consequently, great effort has been put into experimental rock mechanics and to analogue and theoretical modelling of rock behaviour, with particular attention being paid to the use of geometrical patterns in deformed rocks as constraints on rock rheology (e.g. Passchier et al., 1993; Hudleston and Lan, 1994; Schmalholz and Podladchikov, 2001). Special attention has been paid to mylonitic shear zones and to the geometry of their constituents, because they play an important role in the accommodation of shear movement in the lithosphere. However, rock behaviour in mylonite zones is complex, especially the rheology of these high-strain rocks as reflected in the flow around strong or rigid inclusions, and there is still disagreement concerning theoretical and experimental models. For instance, Cox et al. (1968) and Masuda and Ando (1988) came to the theoretical conclusion that the flow of a Newtonian viscous matrix around a circular rigid inclusion in simple shear has an eye-shaped pattern (Fig. 1A). On the other hand, Passchier et al. (1993) concluded from a series of experimental studies that the type of flow (eye- or bow tie-shaped) depends on the nature of the viscous matrix (Newtonian or power-law, respectively). However, Masuda and Mizuno (1996) concluded theoretically that the nature of the matrix does not influence the type of flow, which in their analysis is always eye-shaped. Bons

---

* Corresponding author. Tel.: +351-217500000; fax: +351-217500064
E-mail address: fmarques@fc.ul.pt (F.O. Marques).

0191-8141/$ - see front matter © 2005 Elsevier Ltd. All rights reserved.
doi:10.1016/j.jsg.2004.11.005

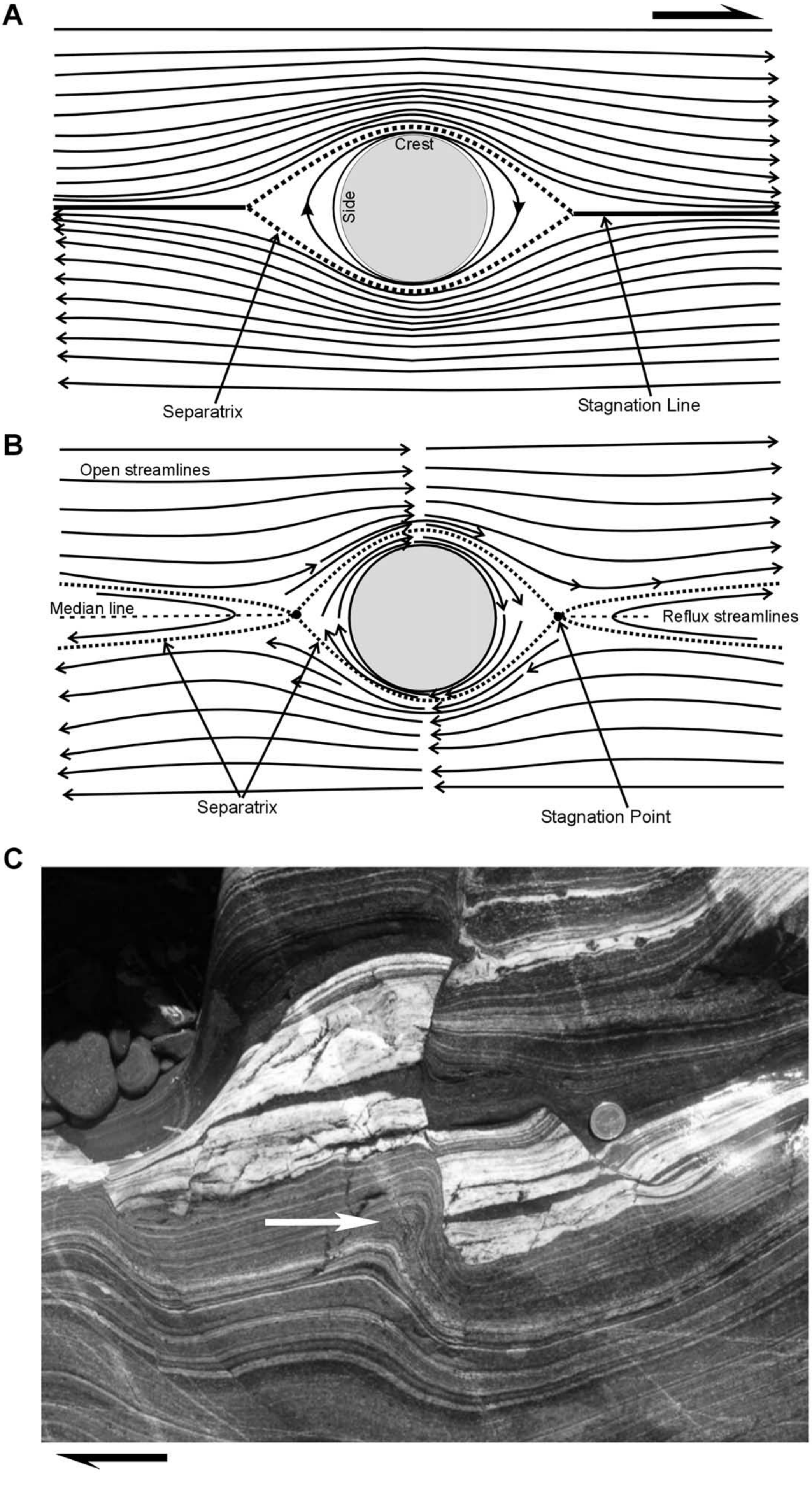
A
Crest
Side
Separatrix
Stagnation Line
B
Open streamlines
Median line
Reflux streamlines
Separatrix
Stagnation Point
C

et al. (1997) and Pennacchioni et al. (2000) concluded from theoretical studies that the Newtonian or non-Newtonian (power law) character of the viscous fluid does not significantly affect the flow pattern around a rigid circle, but while Pennacchioni et al. (2000) obtained a flow pattern that always had a bow tie shape (Fig. 1B), Bons et al. (1997) concluded that the boundary conditions for approximately simple shear can determine the characteristics of the flow field around an inclusion, and eye- and bow tie-shaped patterns are possible. Note that all these studies on flow around rigid inclusions only considered circular inclusions.

Eye- and bow tie-shaped patterns are illustrated in Fig. 1. The eye-shaped pattern is characterized by: (i) closed streamlines around the inclusion, with an elliptical (eye) shape away from the inclusion and tending to become circular close to it; (ii) open streamlines elsewhere in the model domain, rectilinear away from the inclusion and bulging when around it; (iii) an eye-shaped separatrix between open and closed streamlines (the separatrix is a line separating open from closed streamlines); (iv) two stagnation lines (null velocity), one at each side of the inclusion and on the median line (*X*-axis), starting at the tip of the outermost closed streamline. This flow pattern may exist in incompressible fluids if the shear zone width is infinite or if velocity components normal to the shear direction are allowed in the far field flow (e.g. Masuda and Ando, 1988; Masuda and Mizuno, 1996; Bons et al., 1997). The bow tie-shaped pattern is characterized by: (i) closed streamlines around the inclusion, with an elliptical (eye) shape in the outermost cells and changing to circular inwards; (ii) reflux streamlines at the sides of the inclusion, with two distinct halves, one on each side of the median line, with opposite velocity components along the shear direction; (iii) open streamlines passing at the inclusion crests (inclusion portions facing shear zone walls), rectilinear away from the inclusion and bulging when around it; (iv) a bow tie-shaped separatrix between open and closed streamlines and between open and reflux streamlines; (v) two stagnation points on the median line, one to each side of the inclusion, between closed and reflux streamlines.

Strain localization is commonly observed in mylonites in the form of shear bands of variable thickness. In layered mylonites (Fig. 1C), layers of different viscosity subject to a constant stress can flow at different rates, with the generation of microscopic/mesoscopic shear zones in which the ratio between their thickness and the rigid inclusion's least dimension can approach one (cf. fig. 4c in Marques and Cobbold, 1995). Marques and Cobbold (1995) verified experimentally that confinement affects rigid inclusion rotation and investigated the effects on flow of passive markers around the inclusion. Pennacchioni et al. (2000) concluded that the flow around a rigid circle is always bow tie-shaped, and investigated the effects of confinement on the location of stagnation points, but did not present or discuss the effects on flow pattern. Marques and Coelho (2001) analysed the effects of confinement on rotation of elliptical rigid inclusions but not the effects on matrix flow. Biermeier et al. (2001) investigated the effects of confinement on the rotation of a rigid circle, but not the effects on matrix flow. We now follow up the work begun by Marques and Cobbold (1995) and Marques and Coelho (2001) through investigation of the influence of confinement (as indicated by the ratio, *S*, between the width of the shear zone, *H*, and the inclusion's least principal axis. e_2, $S=H/e_2$; Fig. 2A) on matrix flow (see also Biermeier et al., 2001; Samanta et al., 2003), and analyse the results in long and short channels to evaluate the effects of confinement at short and long distances from the inclusion. Note that most (if not all) model domains and figures accompanying works on flow patterns around rigid circles are short range (e.g. Masuda and Ando, 1988; Passchier et al., 1993; Masuda and Mizuno, 1996; Pennacchioni et al., 2000), and most observations carried out in micro-tectonics (analysis of porphyroclast systems for example) are in the same range—commonly less than 10 inclusion diameters. We can, therefore, define an effective channel length and an effective flow pattern. We use analogue and numerical modelling to address these issues.

2. Analogue experiments

We used polydimethyl-siloxane (PDMS—manufactured by Dow Corning of Great Britain under the trade name SGM 36) as the viscous matrix (see Weijermars (1986) for PDMS properties), and Plexiglas as the rigid inclusion. The experiments were carried out in the shear box described in Marques and Coelho (2001). The shear box has a vertical shear plane, and comprises two horizontal fixed upper and lower walls (normal to the shear plane), two vertical side walls (parallel to the shear plane), one fixed and the other motor-driven, and two vertical top walls articulated with the side walls to keep the volume constant and maintain the model's geometry. To ensure homogeneous simple shear flow in the model, PDMS adheres perfectly to the lateral walls (which transmit simple shear flow to PDMS), and a neutral liquid soap is used to ensure free slip on all other walls. In this way, simple shear flow is homogeneous

Fig. 1. (A) and (B) Schematic representations of perturbation of streamlines around a rigid circle in the *XZ* plane. (A) Eye-shaped pattern. (B) Bow tie-shaped pattern. (C) Photograph of a natural example of a layered mylonite from the Bragança Massif, NE Portugal, which is a mafic granulite deformed and retrogressed to amphibolite facies. Note that, for the same PT conditions, layers behave quite differently. For instance, while the darker amphibole-rich layers deform by folding (white arrow), the lighter plagioclase-rich layer deforms by fracturing. A similar situation is observed with layers still rich in high-grade metamorphic minerals like pyroxene and garnet. This strain partitioning between adjacent layers can concentrate shear deformation in narrow, softer bands inside the wider shear zone, and lead to confined flow. See Marques et al. (1996) for the geological setting. Sense of shear is top to the right (West).

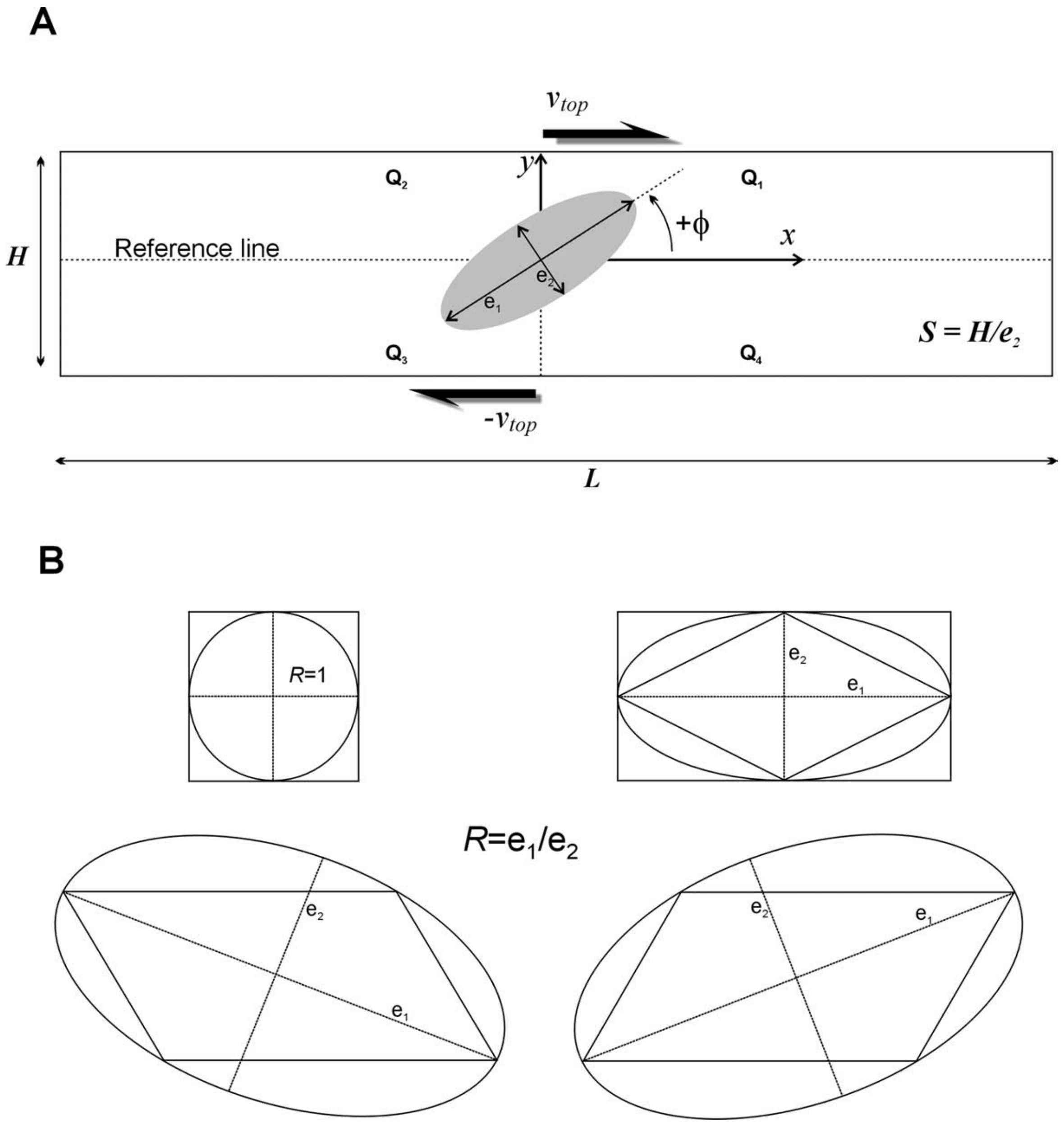

Fig. 2. (A) Representation of the computational domain with an elliptical inclusion. H and L are the height and length of the domain; e_1 and e_2 are the principal axes of the elliptical inclusion; ϕ is the angle between e_1 and X, and is positive anticlockwise; Q_n are quadrants from 1 to 4. The shear direction is parallel to the X-axis and the sense of shear is top to the right in all figures. (B) Shapes used in this study and respective aspect ratios (R). Shapes are not drawn to scale.

throughout the model and is only driven by the lateral walls. The width (H) of the initial rectangular experimental shear zone was 80 mm, the length (L) 500 mm and the depth 30 mm in the case of the circular inclusion with $R=10$ mm (Fig. 2A), and 240, 500 and 30 mm, respectively, in the case of the circular inclusion with $R=4$ mm, which gives S values of 4 and 30, respectively.

We subjected the PDMS parallelepipeds with the embedded inclusions to parallel-sided simple shear, and the results are shown in Fig. 3. The strain rate ($\dot{\gamma}$) used in the experiments was 6.25×10^{-5} s^{-1}, which falls in the Newtonian field of PDMS as defined by Weijermars (1986). Before starting the experiment, we stamped the surface of the PDMS with a passive grid of black dots to be able to follow displacements in the viscous matrix. The displacement paths shown in Fig. 3 were obtained by superimposing photographs of successive stages at regular γ intervals and drawing arrows that represent the change of position of individual dots. Fig. 3 reveals clear bow tie-shaped patterns. The stagnation points (marked by white dots in Fig. 3) are close to the inclusion perimeter in the case of $S=4$ (Fig. 3A) and further from the inclusion in the case of $S=30$ (Fig. 3B). We estimated the position of the stagnation points as the ratio D between the abscissa of the

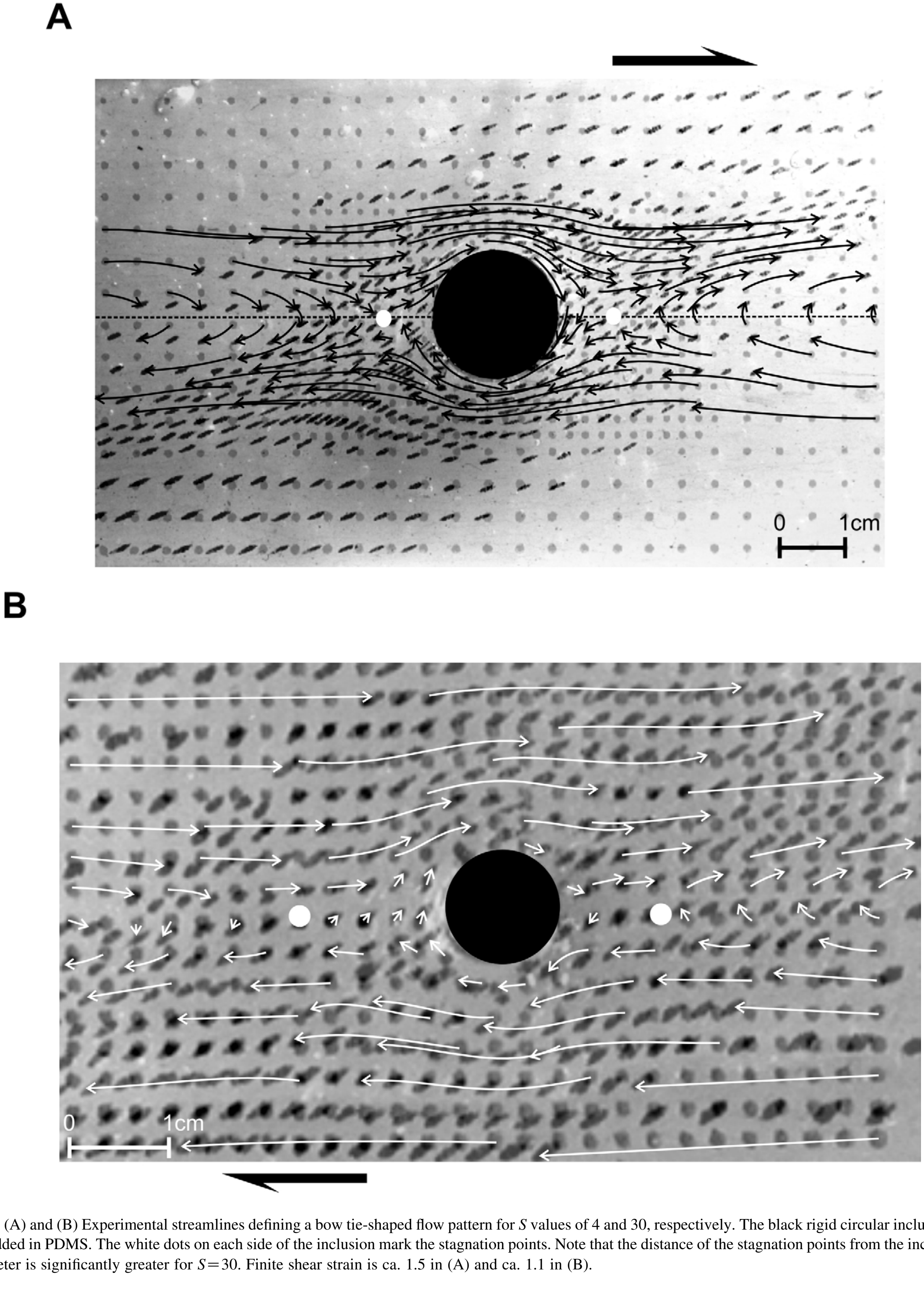

Fig. 3. (A) and (B) Experimental streamlines defining a bow tie-shaped flow pattern for S values of 4 and 30, respectively. The black rigid circular inclusion is embedded in PDMS. The white dots on each side of the inclusion mark the stagnation points. Note that the distance of the stagnation points from the inclusion perimeter is significantly greater for $S=30$. Finite shear strain is ca. 1.5 in (A) and ca. 1.1 in (B).

stagnation point and the circle radius, which is ca. 1.8 for $S=4$ and 3.6 for $S=30$.

3. Model formulation

3.1. Governing equations and boundary conditions

Incompressible viscous fluid rheology is widely accepted in the literature as a simple but effective approximation to the behaviour of rocks undergoing ductile deformation. In the case of steady-state motion of a viscous, incompressible Newtonian fluid at very low Reynolds number, the dynamical Navier–Stokes flow equations reduce to the Stokes approximation. The mathematical model used in the present work is based on the two-dimensional (2-D) steady-state incompressible Navier–Stokes equations (Granger, 1994):

$$\rho\left(\frac{\partial \mathbf{u}}{\partial t} + \mathbf{u}\cdot\nabla\mathbf{u}\right) = -\nabla p + \eta\nabla^2\mathbf{u} + \mathbf{F} \tag{1}$$

$$\nabla\cdot\mathbf{u} = 0 \tag{2}$$

where $\mathbf{u}$ is the velocity vector, p the pressure, ρ the density, η the dynamic viscosity and $\mathbf{F}$ the external body force (ρ and η are constant and $\mathbf{F}$ will be assumed negligible in this model). Then, defining the scaled variables $\bar{\mathbf{x}}=\mathbf{x}/L$, $\bar{\mathbf{u}}=\mathbf{u}/U$, $\bar{p}=p/P$ and $\bar{t}=t/T$, in terms of the characteristic length L, velocity U, pressure P and time $T=L/U$, Eqs. (1) and (2) become:

$$\frac{\partial \bar{\mathbf{u}}}{\partial t} + \bar{\mathbf{u}}\cdot\nabla\bar{\mathbf{u}} = -\mathrm{Eu}\bar{p} + \frac{1}{\mathrm{Re}}{}^{2}\bar{\mathbf{u}} \tag{3}$$

$$\bar{\ }\cdot\bar{\mathbf{u}} = 0 \tag{4}$$

where $\mathrm{Re}=\rho UL/\eta$ and $\mathrm{Eu}=P/\rho U^2$ are, respectively, the Reynolds and Euler numbers. For flows at low characteristic velocity U and high viscosity η, we have $\mathrm{Re}\ll 1$ and $\mathrm{Eu}>>1$, and all inertial terms in Eq. (3) become negligible. We thus obtain the Stokes approximation of the momentum equation for quasi-static (creeping) flows, which in dimensional form reads:

$$-\nabla p + \eta\nabla^2\mathbf{u} = 0 \tag{5}$$

The boundary conditions needed to complete the mathematical formulation and define a simple shear flow were (i) velocity at $Y=\pm H/2$ set to values $\pm V_{\mathrm{top}}$ in order to induce a vorticity value of -1 in the far field flow, (ii) velocity set to vary linearly between top and bottom velocities (with zero-mean) at left and right end boundaries (straight-out condition), and (iii) no-slip condition at the interface between inclusion and matrix. The inclusion's rotation rate is a direct consequence of these boundary conditions. In the particular case of the circle, and for direct comparison with the analogue experiments, (i) the matrix viscosity was taken equal to the viscosity of PDMS (5×10^4 Pa s), (ii) the width (H) and length (L) of the computational domain were set equal to the experimental domain, (iii) the velocities at the top and bottom boundaries were set equal to the experimental velocities, (iv) the velocity was set to vary linearly (with zero-mean) at the left and right boundaries, and (v) a perfect adherence condition at the inclusion–matrix interface was assumed.

The flow equations were solved using the finite-element program FEMLAB (2002) developed by Comsol, which runs in MATLAB software. The flow equations, with the specified boundary conditions, were solved in the primitive variables $\mathbf{u}\equiv(u, v)$ and p over a finite element mesh, using the algorithm for stationary incompressible Navier–Stokes flows implemented in FEMLAB. Further details on the computational method and numerical procedures are provided by Gresho and Sani (2000), as well as in the above-mentioned reference.

3.2. Model settings

The above equations were solved for the 2-D rectangular domain illustrated in Fig. 2A, which was filled with an incompressible linear viscous fluid with matrix viscosity (μ) set to one. High-viscosity fluid-modelled inclusions ($\mu=1.0e+6$) or solid inclusions were positioned at the centre of the domain (x, $y=0$). The width (H) of the computational domain was chosen according to the desired confinement ($S=H/e_2$). The length (L) was set to at least 40 times the inclusion longest axis (e_1). The angle between the instantaneous direction of e_1 and the shear direction (X) is the inclusion orientation (ϕ), which is positive counterclockwise.

The inclusion shapes studied were ellipses, rectangles, lozenges and skewed rectangles (Fig. 2B), with aspect ratios ($R=e_1/e_2$) equal to 1, 1.5, 3 and 6, to simulate most of the basic shapes found in natural shear zones. To determine the rectangle R we found the ratio between the long and short sides (inscribed ellipse as in Ghosh and Ramberg (1976)), and for the lozenge and skewed rectangles we used the aspect ratio of the circumscribed ellipse. In this case, the ellipse's longest axis is inclined relative to X when the long sides of the inclusion are parallel to X.

4. Numerical results

The reliability of the numerical procedure was tested using analytical results obtained for a circular inclusion (Jeffery, 1922). We used a large S value ($S=30$) and the result agrees remarkably well with the analytical solution. The circular rigid inclusion rotated at a constant ω in the numerical model, equal to $0.5\dot{\gamma}$ (or $0.5W$) as predicted by Jeffery (1922).

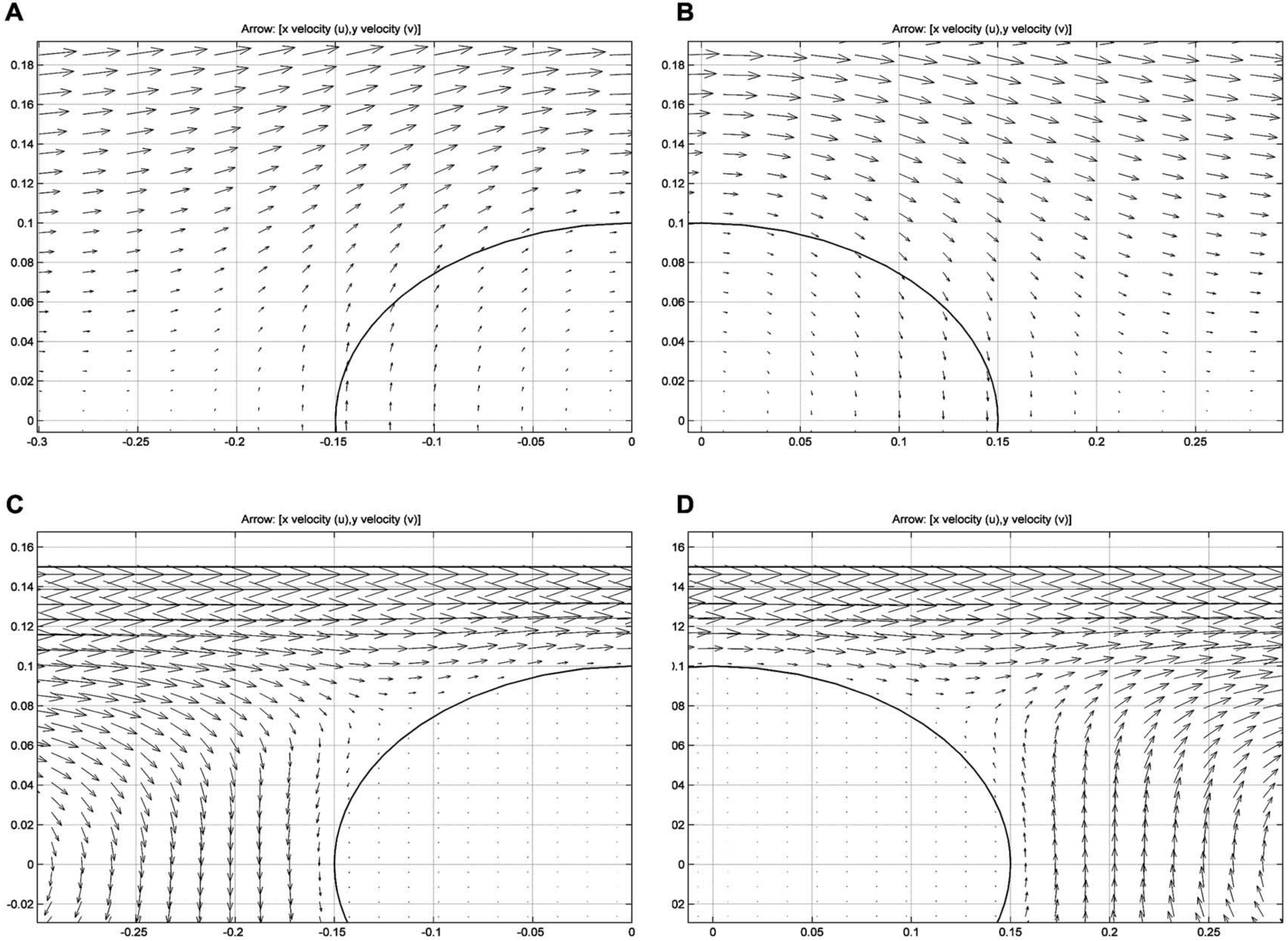

Fig. 4. Velocity vector fields close to the inclusion for $S=10.0$ ((A) and (B)) and $S=1.5$ ((C) and (D)). Sense of shear is top to the right.

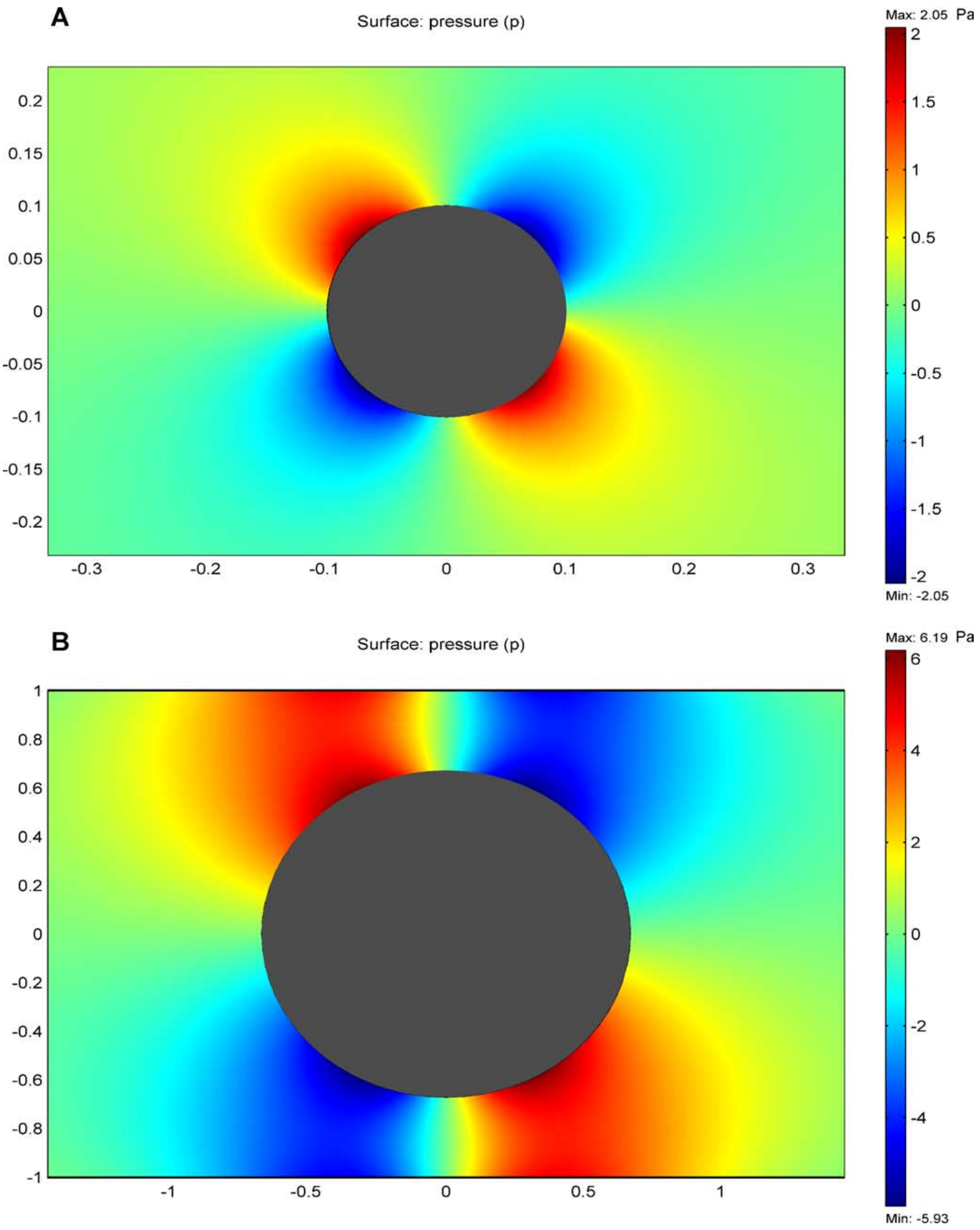

Fig. 5. Colour maps to illustrate confinement effects on pressure for the circle at $S=10.0$ (A) and $S=1.5$ (B). Sense of shear is top to the right.

4.1. Velocity

The velocity vector fields are illustrated in Fig. 4. We show the example of the ellipse with aspect ratio equal to 1.5 because it is quite illustrative of the influence of the rigid inclusion and of the effects of confinement on the nearby flow. Inclusion shape also plays an important role, which will be apparent in the streamline maps presented below. The degree of influence decreases with increasing distance from the rigid body, and flow far from the inclusion (especially in the Y direction) is homogeneous simple shear. The rotation behaviour of a rigid elliptical inclusion in confined flow is analysed by Taborda et al. (2004).

When confinement is small ($S>10$), the X-component of the velocity field is always positive in the matrix in the upper half of the model (Fig. 4A and B) and negative in the lower half, in agreement with the applied far field velocity and matrix vorticity. On the other hand, when flow is confined, e.g. $S=1.5$ (Fig. 4C and D), there are regions around the inclusion where the X-component of the velocity field is negative in the upper half and positive in the lower half, i.e. where there is back-flow. When $S>10$, the Y-component of the velocity field close to the inclusion is always positive in Q_2 (Fig. 4A) and Q_3, and negative in Q_1 (Fig. 4B) and Q_4. When S is small, the Y-component of the velocity

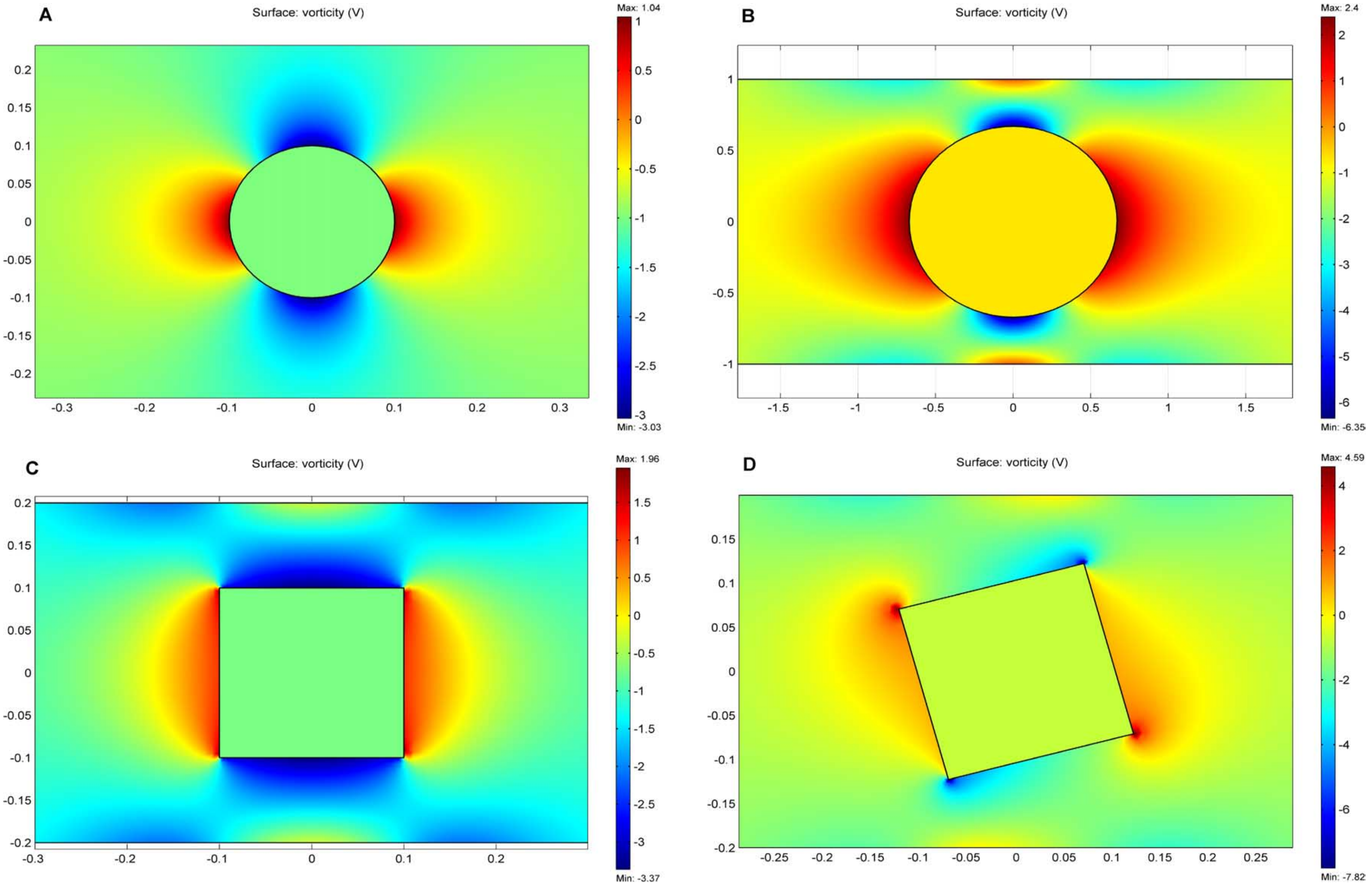

Fig. 6. Colour maps to illustrate confinement effects on vorticity for the circle at $S=15.0$ (A) and $S=1.5$ (B), and to show the changes in vorticity configuration and magnitude with ϕ ((C) and (D)). Sense of shear is top to the right.

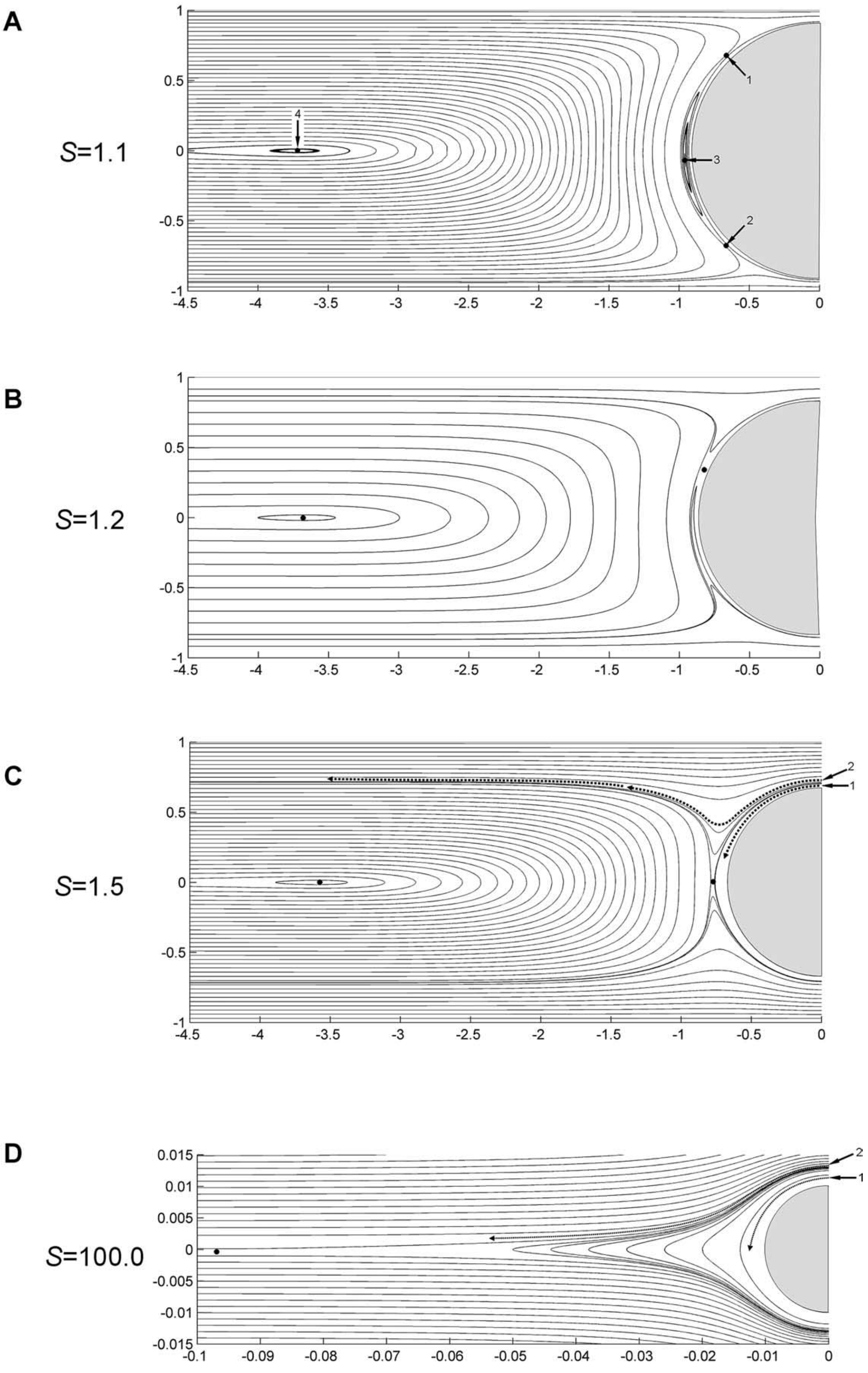

Fig. 7. Flow maps for increasing *S* values. Note the considerable changes in flow pattern, which induce migration of stagnation points (marked by black dots and numbered in (A)) and of vortexes. In (C) and (D) we added the trajectories of material particles to evaluate the degree of stair-stepping. Sense of shear is top to the right in (A) and (B), and top to the left in (C) and (D).

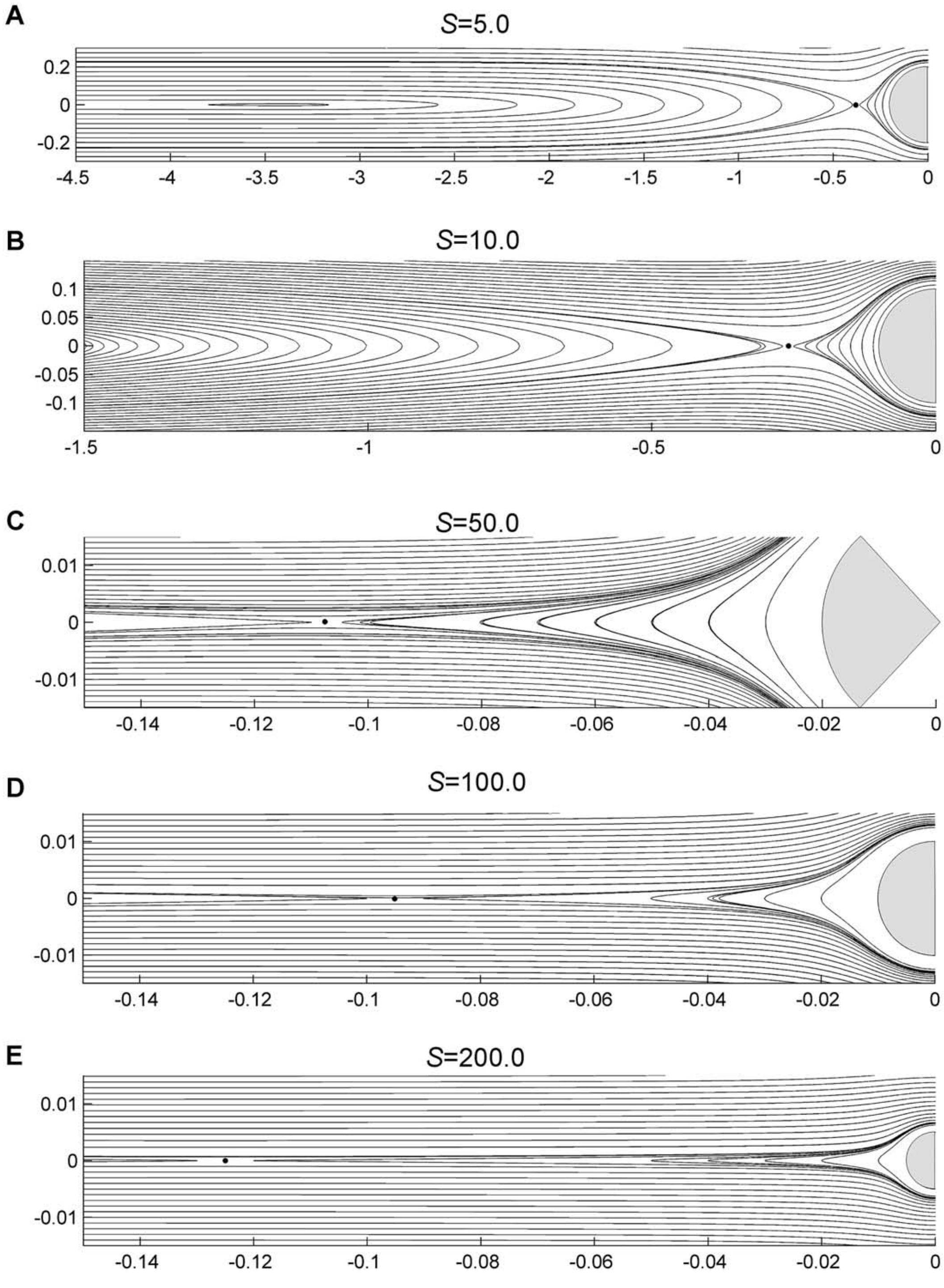

Fig. 8. Flow maps for increasing *S* value to show the significant migration of stagnation points (marked by black dots). Sense of shear is top to the right.

field close to the inclusion is negative in a large part of Q_2 (Fig. 4C) and Q_3, and positive in a large part of Q_1 (Fig. 4D) and Q_4.

4.2. Pressure

The pressure fields are illustrated in Fig. 5. As could be expected from the type of far field flow and the circular shape of the rigid inclusion, the pressure distribution around the rigid inclusion is anti-symmetrical relative to the *X*- and *Y*-axes, with peaks half way between those axes and null pressure on the axes when *S* is large. As *S* tends to one (Fig. 5B), significant changes occur in the distribution and magnitude of pressure: pressure gradients increase and pressure peaks shift towards the *Y*-axis.

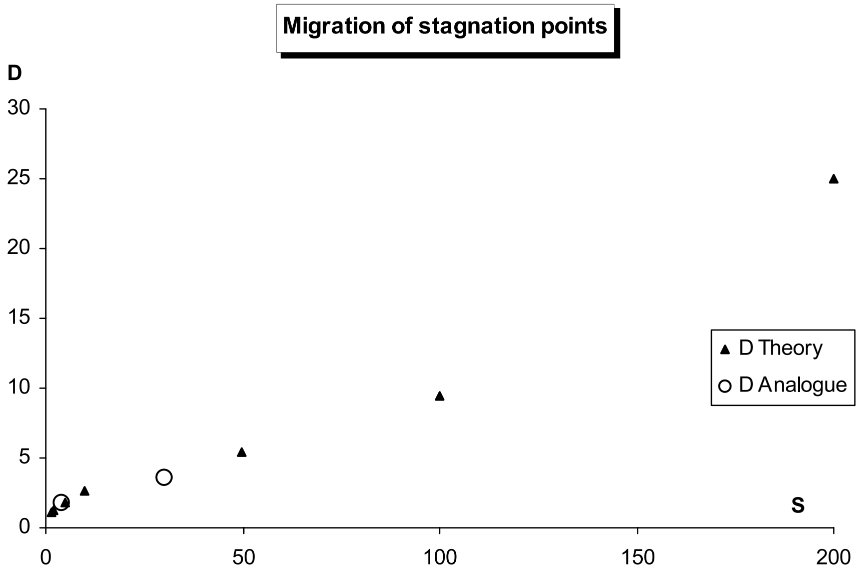

Fig. 9. Graph to illustrate migration of stagnation points with S. Note that the experimental data are in close agreement with the numerical results.

4.3. Vorticity

The colour maps shown in Fig. 6 were produced to evaluate vorticity in the matrix and inclusion. Vorticity configuration and magnitude in the matrix around the inclusion change markedly with S, and when confinement is effective, inclusion shape, aspect ratio and orientation also play an important role.

4.4. Matrix flow

The matrix displacement fields are represented by the streamline plots shown in Figs. 7, 8 and 11–13, which illustrate the way the matrix flows around a rigid inclusion and the effects that confinement may have on flow patterns.

Concerning the circle, the effects with increasing confinement are (Figs. 7 and 8): (1) eye-shaped closed cells around the inclusion tend to a circular shape and shift towards the inclusion perimeter. At $S=1$ these closed cells only exist in a very narrow corona around the inclusion. (2) Reflux streamlines to each side of the inclusion change shape considerably, especially when closer to the inclusion. V-shaped streamlines change to U-shaped, with inwards embayments at the sides of the inclusion when S approaches one. (3) The number of vortexes increases. Two are apparent at $S<5$ in the reflux cells, and two more appear at $S=1.1$ very close to the inclusion, one at each side, between the closed cells surrounding the inclusion and the reflux streamlines. (4) With increasing S, the stagnation points between the reflux streamlines and the closed cells around the inclusion move away from the inclusion, as shown in Figs. 7 and 8 and by the graph of Fig. 9. (5) The number of stagnation points increases. For $S>20$, there are no closed cells at the sides of the inclusion (at least to distances of about 100 inclusion diameters). Therefore, only two stagnation points exist, one to each side of the inclusion and on the X-axis (as given in the definition and shown in Figs. 7 and 8). With confinement, the flow becomes more complex and vortexes form at the sides of the inclusion, close to and away from it, thus generating more stagnation points. At $S=1.1$, there are eight stagnation points (Fig. 7A). (5) Open flow lines passing at the inclusion crests become straighter in most of their length, except for two regions close to the inclusion where embayments form, whose depth increase with confinement. The effective eye-shaped pattern observed in our model for $S=200$ shows that closed cells around the inclusion can reach as far as 12 inclusion diameters.

Concerning other inclusion shapes (ellipse, square, rectangle, lozenge and skewed rectangles), we will only consider the square, ellipse and lozenge for description of matrix flow, because for the other shapes no significant differences were observed. For inclusions with $R>1$, and in contrast to the circle, the presented ‘streamlines’ are not streamlines sensu strictu, because they are instantaneous or only valid for a short inclusion rotation. Anyway, for the case of the square we give the velocity fields for three different orientations (Fig. 10) as background for the ‘streamline’ maps (Figs. 11–13). For $S=15$ (Fig. 11), the flow pattern around all the shapes is similar to the case of the circle. The exceptions are the skewed rectangles, which show a slight asymmetry relative to X at the sides of the inclusions and a migration of the stagnation points towards the inclusion perimeter. With regard to the square at $\phi=0°$, the effects on flow with increasing confinement are similar to the circle, but the vortexes close to the inclusion sides were not observed. Therefore, only four stagnation points were observed. With inclusion rotation, however, and unlike the circle, the geometry changes and so does the flow pattern. At $\phi=0°$ and $S=1.5$ (Fig. 12A), the flow pattern is

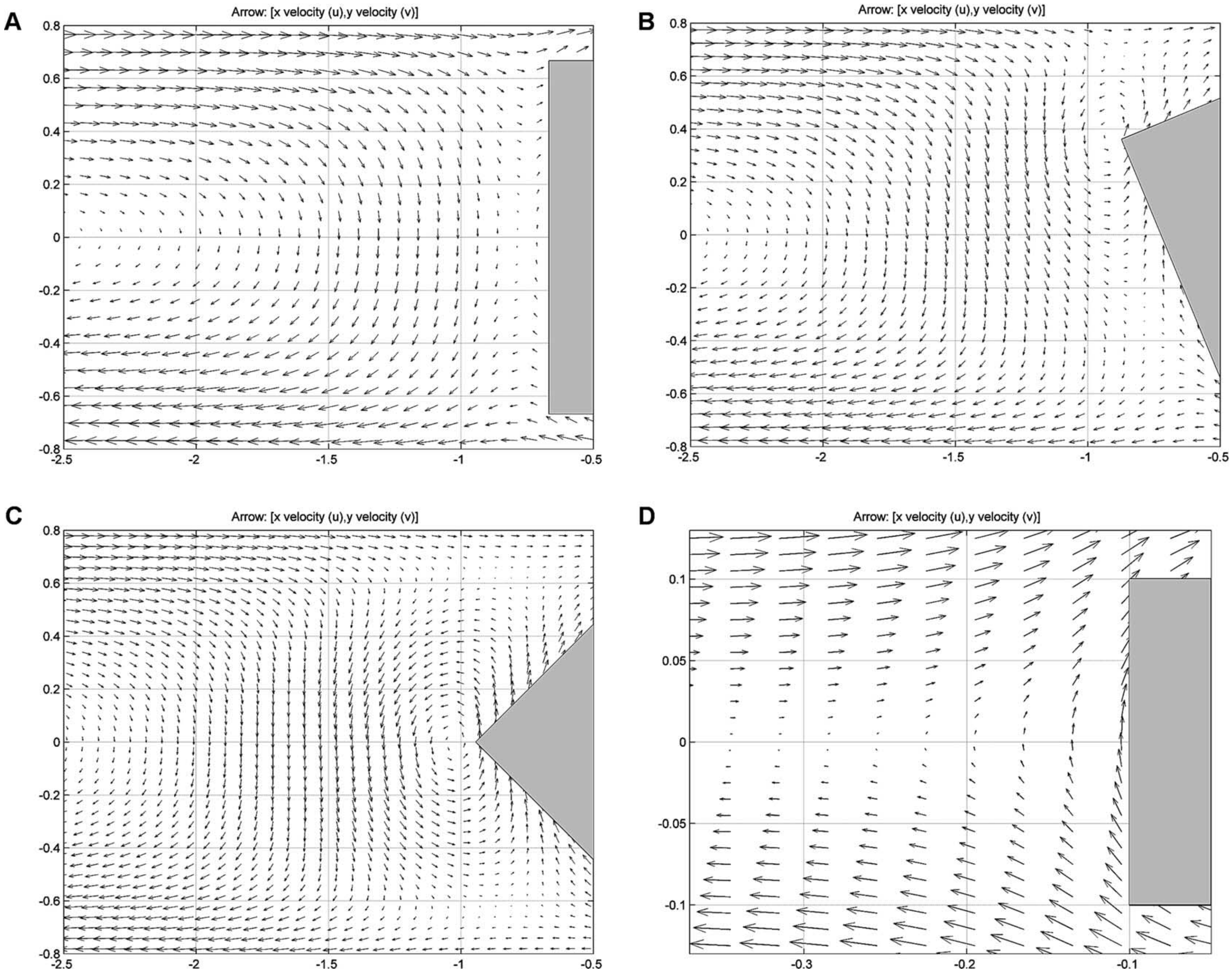

Fig. 10. Velocity vector fields for the square at $S=1.5$ ((A)–(C)) and $S=15$. Note the considerable variations with confinement and with square orientation, and also the circular cells at the square corners. (A) $\phi=0°$; (B) $\phi=22.5°$; (C) $\phi=45°$. Sense of shear is top to the right.

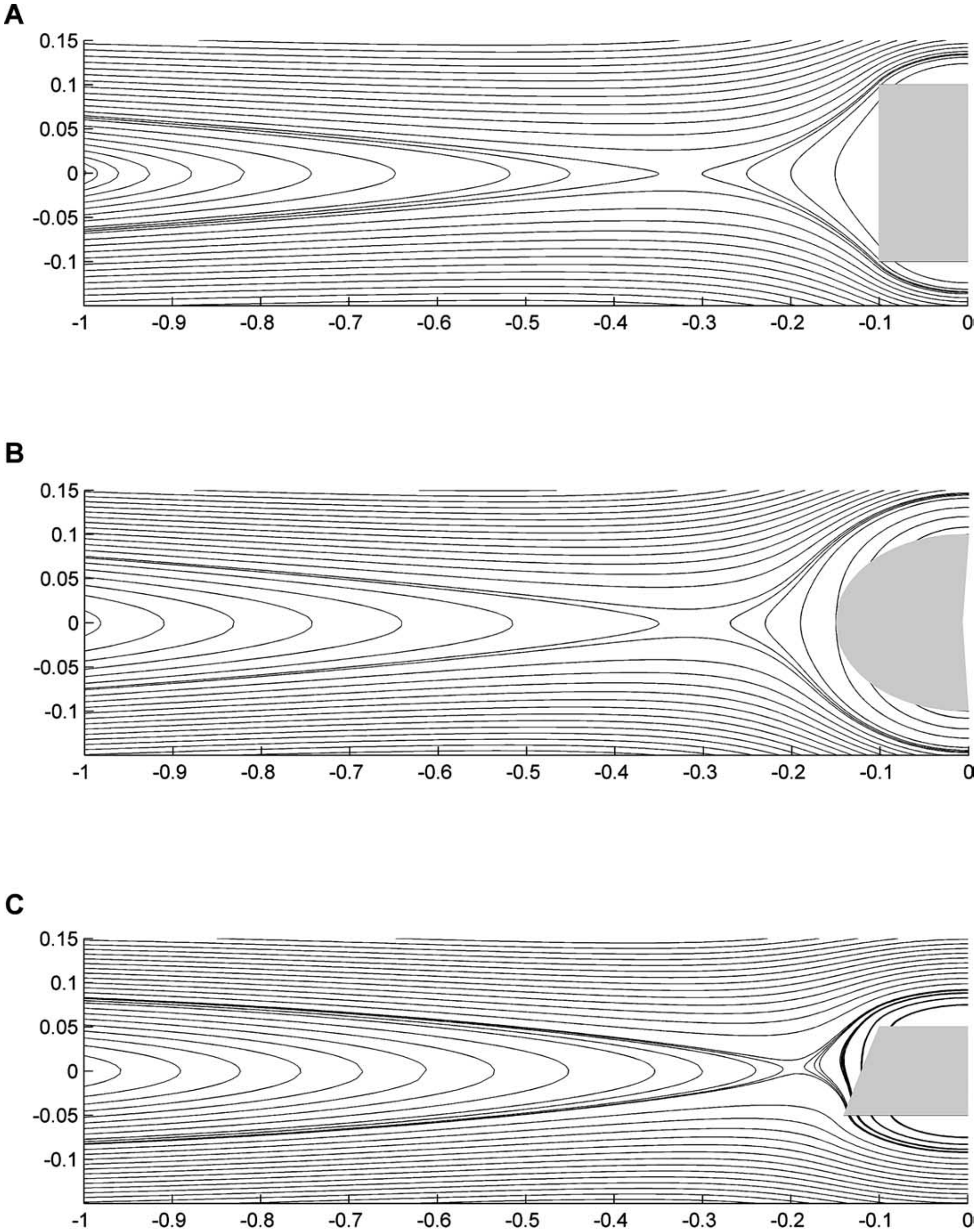

Fig. 11. ‘Streamline’ maps for square (A), ellipse (B) and skewed right rectangle (C) at $S=15$ and $\phi=0°$. Note the similarity of (A) and (B) to the circle. Note also the asymmetry of the ‘streamlines’ and the migration of the stagnation point towards the inclusion perimeter in the skewed rectangle. Sense of shear is top to the right.

still similar to the case of the circle. From $\phi=0$ to 22.5° at $S=1.5$ (Fig. 12B), the flow pattern undergoes major modifications: it becomes strongly asymmetrical relative to X, and two vortexes arise at the upper left and lower right corners of the square. From $\phi=22.5$ to 45° at $S=1.5$ (Fig. 12C and D), the vortexes change corners and at $\phi=45°$ symmetry relative to X is re-established. For $\phi=22.5$ and 45° at $S=1.5$, eight stagnation points must exist. A similar pattern is observed for the lozenge at $\phi=90°$, and similar behaviour is observed in the rectangle and skewed rectangles during a whole revolution. Regarding the ellipse and the lozenge at $S=1.5$, the flow patterns are similar at $\phi=30°$ but significantly different at $\phi=60°$. At $\phi=30°$ (Fig. 13A), the flow patterns close to the inclusion are strongly asymmetrical relative to X and only four stagnation points are observed. At $\phi=60°$, the flow patterns close to the lozenge regain symmetry relative to X, and the flow pattern close to the ellipse (Fig. 13B) becomes more asymmetrical.

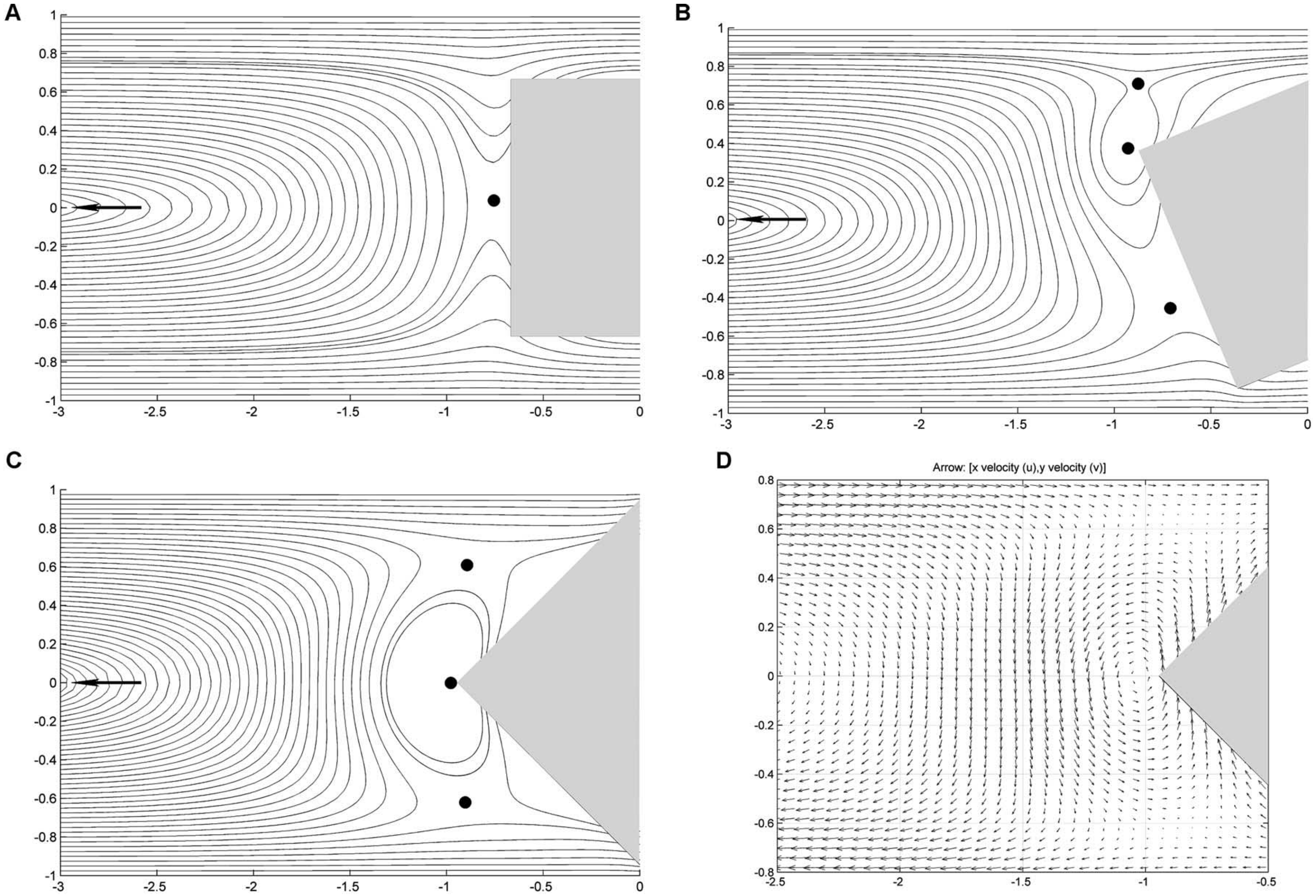

Fig. 12. ‘Streamline’ maps for the square at $S=1.5$ and for $\phi=0°$ (A), $\phi=22.5°$ (B) and $\phi=45°$ (C), and velocity vector field for comparison (D). Note the significant variations with inclusion orientation and migration of vortexes. Arrows indicate position of the vortexes outside the picture, and black dots mark the position of stagnation points. Sense of shear is top to the right.

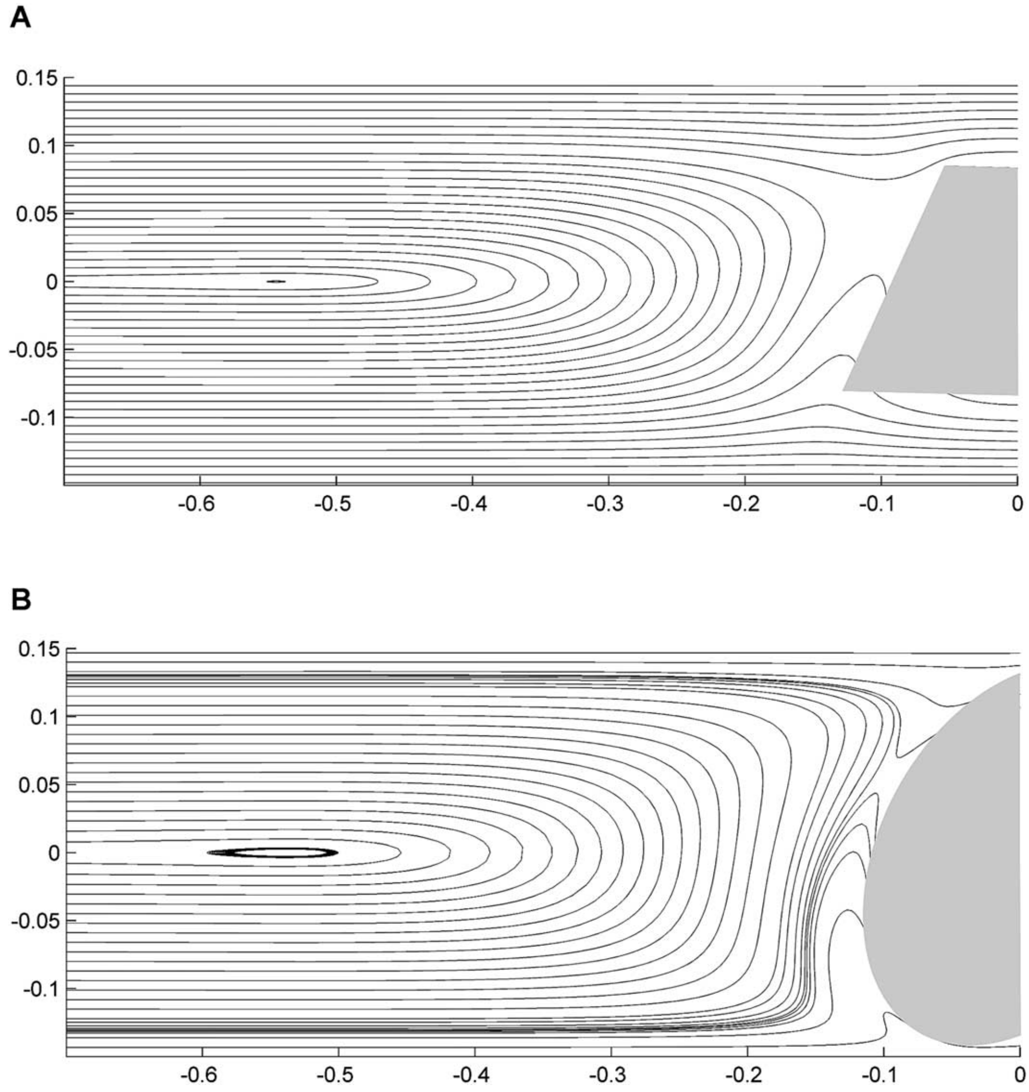

Fig. 13. 'Streamline' maps for the lozenge at $S=1.5$ and $\phi=30°$ (A), and for the ellipse at $S=1.5$ and $\phi=60°$ (B). Sense of shear is top to the right.

5. Discussion and conclusions

When we compare the present results with the classic eye- and bow tie-shaped patterns for rigid inclusions in non-slipping contact with a viscous matrix, significant differences stand out as to the bow tie-shaped pattern: (1) for $S<5$ two vortexes arise in the middle of the reflux streamlines and centred on the X-axis, which doubles the number of stagnation points observed in the definition. At $S=1.1$ two more vortexes appear close to the inclusion, which multiplies the number of stagnation points by four. (2) The open reflux streamlines become closed cells for $S<5$. (3) With increasing S, the stagnation points either disappear or move away from the inclusion. At very small S values, the flow pattern becomes even more complex and the classic separatrix changes configuration. The stagnation points close to the inclusion seem to result from the interaction between flow in the matrix and inclusion rotation. Stagnation points within closed circuits (3 in Fig. 7A) result from opposite senses of flow, and stagnation points like 1 and 2 in Fig. 7A appear in the boundary between closed and open flow lines. Concerning the eye-shaped pattern, there are minor differences between our model and the classic definition. Note, however, that closed cells around the inclusion can reach as far as 12 inclusion diameters for $S=200$. This may have a considerable influence on the geometry of tails around the inclusion.

Despite the facts that, in our analogue and numerical models, (i) the flow is homogeneous simple shear, (ii) that the fluid used is Newtonian viscous, and (iii) we use a parallel-sided model shear zone, the flow pattern obtained has the shape of a bow tie, in contrast to the models of Cox et al. (1968), Masuda and Ando (1988), Passchier et al. (1993) and Masuda and Mizuno (1996). However, our results are, at least partially, in agreement with those of Bons et al. (1997) and Pennacchioni et al. (2000). In the present study, the results of numerical computations are supported by experimental analogue results. The positions of the stagnation points are in good agreement with the numerical results (Fig. 9). The numerical model shows that the flow pattern in a viscous Newtonian matrix around a circular rigid body depends strongly on S; in long channels and in strict terms, the flow pattern is bow tie-shaped, but tends to become eye-shaped with increasing S. In terms of comparison with structures occurring in natural mylonites, we concentrate our attention on the flow in the neighbourhood of the rigid inclusion, commonly less than 10 inclusion diameters, because structures associated with the inclusion tend to occur within this range. Under these circumstances, we can define an effective channel length and, consequently, an effective flow pattern. The effective flow pattern has a prominent bow tie shape for $S<20$, but is, for all practical purposes, effectively eye-shaped for S values greater than 50. This may have great influence on the geometry of tails around the rigid inclusion. For both short and long distance observations, we may say that, if recrystallization tails form around the inclusion, the degree of stair-stepping (i.e. the step-like distribution of tails around the inclusion relative to the reference plane) depends on S, because the flow pattern depends on the degree of confinement. Note that the degree of stair-stepping for $S=1.5$ should be greater than for $S=50$, and even greater than for $S=100$, because the reverse flow cell is thinner for higher S and, therefore, the open flow lines passing close to the inclusion crests can go closer to the reference plane. To illustrate this, in Fig. 7C and D we show the trajectories that particles of recrystallized material would follow if the rigid inclusion had a mantle with rheology similar to the matrix.

It is interesting to note that the flow type is more sensitive to S than is the rotation rate of the inclusion. For $S>5$ the rotation rate is no longer appreciably affected by confinement, although the flow pattern only changes from bow tie- to eye-shaped at a much higher S value.

Can matrix rheology be inferred from flow patterns around a rigid circular inclusion in simple shear? The answer to this long-standing question has been partly answered by Bons et al. (1997) and Pennacchioni et al. (2000), and we now add the significant role that confinement can play. The present study shows that the same Newtonian viscous fluid can flow around a rigid circle with effective eye- or bow tie-shaped patterns, depending on the degree of confinement. We conclude that one must be very cautious when trying to infer rock rheology from model flow patterns. In the case of natural structures, we should be even more cautious because the flow pattern can only be tentatively inferred from geometrical features. For instance, porphyroclast systems, a pervasive structure found in mylonite zones, commonly exhibit stair-stepping of tails, a geometrical feature that could be related to the type of flow around the inclusion. However, the present study shows that the type of flow depends on S, and previous theoretical work showed that the type of flow is almost independent of matrix rheology (Newtonian or power-law).

Acknowledgements

This is a contribution to research projects GEOMODELS (POCTI/CTA/38695/2001 and POCTI/CTE-GIN/59324/2004) and TEAMINT (POCTI/CTA/48137/2002). Santanu Bose is grateful to CSIR, India, for giving him leave to carry out work at the University of Lisbon. The final version of this paper benefited from the constructive reviews by L. Arbaret and T. Masuda, and editorial work by J. Hippertt. Special thanks are due to Ramon Anton of Dow Corning (Barcelona, Spain) for having made possible the acquisition of the PDMS. Experiments were performed in the Experimental Tectonics Laboratory of LATTEX-FCUL. We thank Paul Covill for having corrected the English.

References

Biermeier, C., Stüwe, K., Barr, T.D., 2001. The rotation rate of cylindrical objects during simple shear. Journal of Structural Geology 23, 765–776.

Bons, P.D., Barr, T.D., ten Brink, C.E., 1997. The development of δ-clasts in non-linear viscous materials: a numerical approach. Tectonophysics 270, 29–41.

Cox, R.G., Zia, Y.Z., Mason, S.G., 1968. Particle motions in sheared suspensions, XXV. Streamlines around cylinders and spheres. Journal of Colloid and Interface Science 27, 7–18.

Davies, G.F., 1999. Dynamic Earth—Plates, Plumes and Mantle Convection. Cambridge University Press, UK.

FEMLAB 2.3 Reference Manual, 2002. Comsol AB, Tegnérgatan 23, SE-111 40 Stockholm, Sweden.

Ghosh, S.K., Ramberg, H., 1976. Reorientation of inclusions by combination of pure shear and simple shear. Tectonophysics 34, 1–70.

Granger, R.A., 1994. Fluid Mechanics. Dover Classics of Science and Mathematics.

Gresho, P.M., Sani, R.L., 2000. Incompressible Flow and the Finite Element Method. Vols. 1 and 2. John Wiley & Sons, New York.

Hudleston, P.J., Lan, L., 1994. Rheological controls on the shapes of single-layer folds. Journal of Structural Geology 16, 1007–1021.

Jeffery, G.B., 1922. The motion of ellipsoidal particles immersed in a viscous fluid. Proceedings Royal Society of London, Series A 102, 161–179.

Marques, F.O., Cobbold, P.R., 1995. Development of highly non-cylindrical folds around rigid ellipsoidal inclusions in bulk simple shear regimes: natural examples and experimental modelling. Journal of Structural Geology 17, 589–602.

Marques, F.O., Coelho, S., 2001. Rotation of rigid elliptical cylinders in viscous simple shear flow: analogue experiments. Journal of Structural Geology 23, 609–617.

Marques, F.O., Ribeiro, A., Munhá, J.M., 1996. Geodynamic evolution of the Continental Allochthonous Terrane (CAT) of the Bragança Nappe Complex, NE Portugal. Tectonics 15, 747–762.

Masuda, T., Ando, S., 1988. Viscous flow around a rigid spherical body: a hydrodynamical approach. Tectonophysics 148, 337–346.

Masuda, T., Mizuno, N., 1996. Deflection of non-Newtonian simple shear flow around a rigid cylindrical body by the Finite Element Method. Journal of Structural Geology 18, 1089–1100.

Nicolas, A., Poirier, J.P., 1976. Crystalline Plasticity and Solid State Flow in Metamorphic Rocks. John Wiley and Sons, Great Britain.

Passchier, C.W., ten Brink, C.E., Bons, P.D., Sokoutis, D., 1993. δ objects as a gauge for stress sensitivity of strain rate in mylonites. Earth and Planetary Science Letters 120, 239–245.

Pennacchioni, G., Fasolo, L., Cecchi, M.M., Salasnich, L., 2000. Finite-element modelling of simple shear flow in Newtonian and non-Newtonian fluids around a circular rigid particle. Journal of Structural Geology 22, 683–692.

Samanta, S.K., Mandal, N., Chakraborty, C., 2003. Flow patterns around rigid inclusions in a multiple inclusion system undergoing bulk simple shear deformation. Journal of Structural Geology 25, 209–221.

Schmalholz, S.M., Podladchikov, Y.Y., 2001. Strain and competence contrast estimation from fold shape. Tectonophysics 340, 195–213.

Taborda, R., Antunes, J., Marques, F.O., 2004. 2-D rotation behavior of a rigid ellipse in confined viscous simple shear: numerical experiments using FEM. Tectonophysics 379, 127–137.

Weijermars, R., 1986. Flow behaviour and physical chemistry of bouncing putties and related polymers in view of tectonic laboratory applications. Tectonophysics 124, 325–358.